# Quantitative Lung Ultrasound Spectroscopy Applied to the Diagnosis of Pulmonary Fibrosis: The First Clinical Study

Federico Mento, Gino Soldati, Renato Prediletto, Marcello Demi, and Libertario Demi, *Member, IEEE*

***Abstract*— The application of ultrasound imaging to the diagnosis of lung diseases is nowadays receiving growing interest. However, lung ultrasound (LUS) is mainly limited to the analysis of imaging artifacts, such as B-lines, which correlate with a wide variety of diseases. Therefore, the results of LUS investigations remain qualitative and subjective, and specificity is obviously suboptimal. Focusing on the development of a quantitative method dedicated to the lung, in this work, we present the first clinical results obtained with quantitative LUS spectroscopy when applied to the differentiation of pulmonary fibrosis. A previously developed specific multifrequency ultrasound imaging technique was utilized to acquire ultrasound images from 26 selected patients. The multifrequency imaging technique was implemented on the ULA-OP platform and an LA533 (Esaote, Florence, Italy) linear-array probe was utilized. RF data obtained at different imaging frequencies (3, 4, 5, and 6 MHz) were acquired and processed in order to characterize B-lines based on their frequency content. In particular, B-line native frequencies (the frequency at which a B-line exhibits the highest intensity) and bandwidth (the range of frequencies over which a B-line shows intensities within −6 dB from its highest intensity), as well as B-line intensity, were analyzed. The results show how the analysis of these features allows (in this group of patients) the differentiation of fibrosis with a sensitivity and specificity equal to 92% and 92%, respectively. These promising results strongly motivate toward the extension of the clinical study, aiming at analyzing a larger cohort of patients and including a broader range of pathologies.**

***Index Terms*— B-lines, *in vivo*, pulmonary fibrosis (PF), quantitative lung ultrasound (LUS).**

## I. Introduction

RESPIRATORY diseases are among the main causes of death and disabilities in the world [1]. A well-known example is represented by the recent COVID-19 pandemic [2]. Another significant group of pulmonary diseases is represented by interstitial lung diseases (ILDs), which comprehend over 100 disorders of the lung that often lead to the fibrosis of this organ. Particularly, idiopathic pulmonary fibrosis (IPF), which represents about 30% of ILDs [3], is one of the most common forms of lung scarring and affects approximately 3 million people in the world [4]. However, since pulmonary fibrosis (PF) can derive also from known secondary causes (contrary to IPF, which is a subgroup of PF whose causes are unknown), the overall number of patients affected by PF is likely higher. This disease is generally characterized by a poor prognosis, also due to the delayed diagnosis, which is particularly common in IPF [5]. Therefore, to begin early treatment and slow down the progression of the disease, a timely diagnosis is fundamental. The high-resolution computed tomography (HRCT) represents the most utilized imaging instrument to derive a PF diagnosis [4], [5]. Nevertheless, the availability of a faster and more accessible preliminary instrumental examination would be extremely useful to better and more rapidly evaluate the state of the lung and direct the patients to the most suitable clinical path.

Lung ultrasound (LUS) currently represents an exploitable resource that is potentially able to satisfy the aforementioned requirements [6]. LUS is indeed a cost-effective, safe, and portable technology that allows real-time imaging. Its clinical relevance has been receiving growing attention only since 1997 [7]. However, the presence of air, whose acoustic characteristics significantly differs from the soft tissues [8], strongly complicates the use of ultrasound technologies. Standard ultrasound imaging is indeed designed to anatomically investigate the human body by assuming a quasi-homogeneous speed of sound. Furthermore, the acoustic impedances of soft tissues and air are extremely different, hence creating an interface (pleural line) having a high reflection coefficient [8], [9]. For this reason, the healthy lung behaves essentially as a perfect reflector. As a consequence, ultrasound waves bounce multiple times between two strong reflectors, i.e., the pleural line and the probe, hence generating the horizontal artifacts known as A-lines [6]. In contrast, when the lung becomes pathological, vertical artifacts called B-lines appear in the reconstructed image. The correlation between the appearance of B-lines and numerous pathological conditions of the lung are largely

Manuscript received May 29, 2020; accepted July 24, 2020. *(Corresponding author: Libertario Demi.)*

Federico Mento and Libertario Demi are with the Department of Information Engineering and Computer Science, University of Trento, 38123, Trento, Italy (e-mail: federico.mento@unitn.it; libertario.demi@unitn.it).

Gino Soldati is with the Diagnostic and Interventional Ultrasound Unit, Valle del Serchio General Hospital, 55032 Lucca, Italy, and also with Fondazione Toscana Gabriele Monasterio, 56124 Pisa, Italy.

Renato Prediletto is with the Institute of Clinical Physiology, National Research Council, 56124 Pisa, Italy, and also with Fondazione Toscana Gabriele Monasterio, 56124 Pisa, Italy.

Marcello Demi is with Fondazione Toscana Gabriele Monasterio, 56124 Pisa, Italy.

Digital Object Identifier 10.1109/TUFFC.2020.3012289

mentioned in the literature [7], [9]–[13]. These pathological conditions are characterized by the partial replacement of the lung volume previously occupied by air with fluids or tissue, consequently decreasing the acoustic impedance mismatch between soft tissues and the lung surface [8], [9]. Particularly, this replacement causes the formation of acoustic channels (or traps) made of media, such as tissue, water, or blood, where ultrasound can propagate, thus generating the aforementioned vertical artifacts [6], [7], [9], [14].

Hypothesis on the origin of B-lines, and their link to the presence of acoustic traps, has been discussed since similar artifacts were observed in a bubbly medium generated by shaking soapy water [15], rigid structures surrounded by a homogeneous medium [16], foamy phantoms [17], and bubbly media [18]. These studies demonstrate that these artifacts cannot be only associated with the presence of very specific anatomical structures of the lung (e.g., interlobular septa). On the other hand, both the pathological lung and the phantoms described in the previously cited literature have in common the presence of acoustic traps. Understanding and characterizing the interaction between ultrasound waves and these traps could explain the generation of B-lines. Indeed, after having partially trapped the energy of the emitted acoustic waves, these traps probably act as secondary ultrasound sources, which gradually reradiate the energy to the probe [16].

Nonetheless, the genesis of B-lines still remains unclear [19]. Consequently, diagnoses today are only based on the visual interpretation of these artifacts and are, thus, subjective and qualitative [9], [18]. The so-called semiquantitative approaches are mainly characterized by counting the vertical artifacts which appear in the image and are particularly spread in the clinical world [20]–[22]. Moreover, the visual recognition of specific ultrasound patterns and the consequent introduction of scoring systems for evaluating the state of the lung have been recently introduced also in the context of the COVID-19 pandemic [23], [24]. Notwithstanding the clear potentiality of LUS in investigating the lung, these approaches remain strictly dependent on the subjective evaluation of physicians.

Therefore, to provide clinicians with objective information, a quantitative characterization of B-lines is needed. Recent studies indeed focused on developing ultrasound imaging techniques designed for the lung, which aim at providing a quantitative measure describing the state of the organ [18], [25], [26]. While the study by Zhang *et al.* [26] was based on measuring the surface wave speed on the lung, Demi *et al.* [18] and Mohanty *et al.* [25] investigated the relationship between the multiple reflections of ultrasound waves occurring within the acoustic traps and the signal received by the transducer [27]. Of particular interest is the characterization of B-lines with respect to their frequency spectrum [18], which could provide an indirect estimation of both size and shape of acoustic traps [28].

PF represents a disease where the alveolar disposition is heterogeneous and completely subverted with respect to its normal structure [28]. Therefore, the acoustic traps are irregularly distributed and have complex and various shapes, differently from other diseases, such as acute cardiogenic pulmonary edema, where the original alveolar distribution is almost entirely preserved [28]. These irregularities in the pleural plane could be potentially characterized by a frequency analysis of B-lines, whose spectrum is expected to have a broad bandwidth when generated by heterogeneously sized and distributed traps such as with PF [16].

In this article, the frequency content of the B-lines observed in 26 patients with lung pathologies is quantitatively evaluated by exploiting the multifrequency approach presented in [18]. In particular, this research investigates the potentiality to discriminate patients affected by PF by exploiting the frequency dependence of B-lines, which is quantified with a new parameter called "total intensity." This parameter provides a measure of the B-line strength independently of the transmitted pressure amplitudes (assuming that no saturation occurs), which are generally different depending on the transmission parameters (e.g., number of transmitting elements, focal point, and center frequency of the emitted pulse).

This article is organized as follows. The utilized equipment and acquisition methods are presented in Section II-A, whereas Section II-B describes the procedure used to extract the total intensity parameter. Section II-C introduces the utilized features and their statistical analysis, whereas Section II-D presents the exploited classifiers. Then, the main results are shown in Section III, and the conclusions are presented with the discussion in Section IV.

## II. Methods

### A. Data Acquisition

A multifrequency approach based on orthogonal subbands centered at different center frequencies (3, 4, 5, and 6 MHz) was implemented with an ULA-OP programmable platform [29], which was used together with an LA533 (Esaote, Florence, Italy) linear-array probe to acquire raw RF data from 26 patients. This specific set of frequencies was adopted following the results obtained from a study on controlled lung-mimicking phantoms, which showed how analyzing B-lines within this frequency range allowed discriminating between phantom types made to model different levels of lung alteration [18], [27]. The utilized probe has a $-6$- and $-12$-dB bandwidth from 3.8 to 12 MHz and from 3.2 to 13.2 MHz, respectively. The maximum of the transducer transfer function is at 8 MHz. A Gaussian pulse having a 2-$\mu$s time length was transmitted for every center frequency, guaranteeing each subband to have a narrow bandwidth, i.e., 1 MHz at $-10$ dB. The amplitude of each pulse was properly defined with respect to the probe bandwidth in order to equalize the pressure outputs. Adopting a strategy based on the transmission of pulses with a narrow bandwidth is indeed fundamental to better detect B-lines and precisely evaluate their frequency spectrum [18]. A dynamic sinc apodization function was utilized. Focal point and maximum imaging depth were set at 2 and 6 cm, respectively. Given that the pleural line generally sits at a depth of about $2 \pm 1$ cm, this choice allowed the analysis of artifacts for depths up to at least twice the depth of the pleural line. The ultrasound signals were transmitted and received by means of a subaperture of 64 elements, which was linearly shifted over

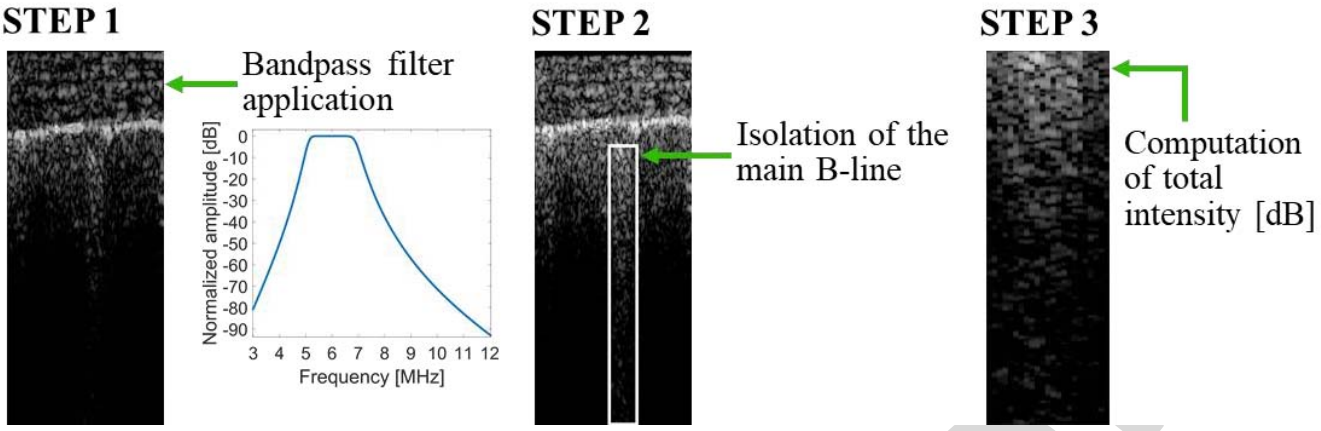


Fig. 1. Procedure applied to the ultrasound data to compute the total intensity of B-lines. In step 1, a sixth-order bandpass Butterworth filter centered at the transmitted center frequency and having a 1.8-MHz bandwidth was applied. In step 2, the obtained image was displayed in logarithmic scale with a 35-dB dynamic range to manually segment the clearest B-line by defining a specific region of interest ($ROI_B$), represented by a white box in the figure (center). In step 3, the total intensity parameter was computed in $ROI_B$ to quantitatively evaluate the B-line strength.

the entire array to reconstruct an image composed of 129 lines. This process was repeated sequentially alternating between the different center frequencies. A pulse repetition frequency (PRF) equal to 4 kHz was utilized. Each image was, thus, formed at a frame rate of PRF/129 = 31 Hz, although a frame rate of 7.75 Hz was obtained when considering the images that belong to the same frequency.

Given the imaging settings described above, the −12-dB lateral resolution measured at focus by means of a wire phantom equals 0.81, 0.66, 0.65, and 0.54 mm when imaging at 3, 4, 5, and 6 MHz, respectively.

The received signals were digitized at a 50-MHz sampling frequency. To increase the signal-to-noise ratio (SNR), the time gain compensation (TGC) was experimentally set by considering the dependence of attenuation on both depth and frequency [30]. A value equal to 1.5 dB/MHz cm was adopted.

The examined patients represent a subgroup of a larger population of 101 patients, who signed an informed consent form to participate in this study (approved by the ethics committee for clinical studies: study number 1089—comitato etico sperimentazione clinica CEAVNO). Subjects consecutively admitted to the Pulmonary Medicine Unit of the Gabriele Monasterio Tuscany Foundation of Pisa in the period November 2017–December 2018 were evaluated. No selection was made for pathology. Subjects younger than 18 years were excluded. During their stay, all subjects underwent thoracic ultrasound by a single operator (GS) with more than ten years of chest ultrasound experience. The patients were not requested to hold their breath during the ultrasound investigation.

Moreover, all patients were investigated for their symptoms according to the procedures usually used in the institution when indicated, without any restriction, at the discretion of the clinician (RP). Instrumental examinations, in addition to the physical examination, were standard radiographs, computed tomography, radioisotopic investigations, and cardiac catheterization. Thoracic ultrasound was performed blindly, and the operator who performed the ultrasound examinations was unaware of the clinical or anamnestic data of the patients. Patients had posterior, basal, paravertebral, and apical scans in a sitting position. In the supine position, front and side scans on all explorable areas, including supraclavicular areas, were acquired. Video clips and RF data of the significant findings were stored.

In this work, to compose a balanced data set, we selected all the patients diagnosed with IPF and an equal number of randomly selected patients without lung fibrosis. Therefore, the investigated subgroup consists of 13 patients (ten males and three females, with age ranging from 56 to 89 years and the mean equal to 76.8) suffering from IPF (Patient ID from 14 to 26) and 13 patients with other diseases (eight males and five females, with age ranging from 55 to 85 years and the mean equal to 74.9), such as chronic obstructive pulmonary disease (COPD) (Patient ID 1, 4, 5, 6, 7, 8, 9, 10, and 13), emphysema (Patient ID 2), pneumonia (Patient ID 3, 4, 7, 13), pulmonary hypertension (Patient ID 8 and 11), and allergic asthma (Patient ID 12). Some of the nonfibrotic patients suffered from multiple diseases. Standard clinical examinations (e.g., CT) were performed to derive these diagnoses.

### *B. Quantification of B-Lines' Intensity*

B-lines' intensity was quantitatively evaluated by exploiting the three-step procedure depicted in Fig. 1. In step 1, to minimize the contributes due to unwanted frequency components, especially the harmonics, a sixth-order bandpass Butterworth filter centered at the transmitted center frequency and having a 1.8-MHz bandwidth was applied. This value was empirically chosen as a tradeoff aimed at minimizing pulse distortion and maximizing noise removal. Moreover, the Hilbert transform was applied to extract the envelope, and the image was normalized with respect to its maximum value (displayed at the pleural line). In this way, the variability introduced by different thickness of intercostal layers on the relative amplitude associated with each B-line artifact (which start at the pleural line) is mitigated. In step 2, the obtained image was displayed in logarithmic scale with a 35-dB dynamic range to visually detect the clearest B-lines over the different imaging

frequencies. Each B-line was then manually segmented by defining a specific region of interest ($\mathrm{ROI}_B$). Given a consecutive block of four images obtained at the four different frequencies, the ROI was manually selected from the image with the largely extended B-line, starting from 3 mm below the pleural line and in order to contain the entire artifact as visualized from a normalized image with a dynamic range of 35 dB. The same ROI was then utilized for the other three images of the block. In the final step, the total intensity parameter was used to quantitatively evaluate the strength of the selected B-lines. First, an arbitrary threshold was set at $-35$ dB, hence considering only the values above the threshold in the computation of the total intensity. This choice was made based on the noise level observed with the data. Then, the total intensity in logarithmic scale was obtained as follows:

$$I_{\mathrm{TOT}} = 20\log_{10}\left(A_{\mathrm{pix}}\sum_{i,j}10^{\frac{\mathrm{ROI}_B(i,j)}{20}}\right) \quad (1)$$

with $A_{\mathrm{pix}}$ being the pixel area (equal to $3.6\times10^{-3}$ mm$^2$), $i$ and $j$ are the indexes referring to the pixel located in $\mathrm{ROI}_B$ at the $i$th row and $j$th column, and $\mathrm{ROI}_B(i,j)$ represents the intensity (in decibels) of the pixel at the $i$th row and $j$th column.

Hence, this new metric introduced the possibility to quantify the relevance of a given B-line by considering both the intensity of the artifact and its spatial extension (implicitly included in the total intensity computation by summing all the pixels contained in $\mathrm{ROI}_B$). Furthermore, thanks to the normalization operation (step 1), the dependence of the total intensity from the received signal amplitudes is mitigated, hence increasing the robustness and the reliability of the analysis.

A total number of 5980 frames (2944 frames acquired from the nonfibrotic group and 3036 frames from the fibrotic group) was processed by means of the aforementioned procedure, leading to the detection of 1029 B-lines.

### C. Features and Statistical Analysis

In this study, we have considered three features, namely the B-line native frequency [18], bandwidth, and total intensity. The first two features correspond to the frequency at which a B-line exhibits the highest intensity and the range of frequencies over which a B-line shows intensities within $-6$ dB from its maximum (when the B-line's intensity is higher than $-6$ dB for all the investigated frequencies, the bandwidth equals to 4 MHz). The total intensity is introduced by (1). For each patient, multiple B-lines were analyzed with respect to these three features.

To represent each patient as a function of native frequency and bandwidth of its B-lines, Gaussian distributions were generated. Specifically, we computed the mean value and the covariance matrix of the native frequency and bandwidth of the B-lines observed in each patient. Successively, for visualization purposes, the covariance matrix was scaled by a factor of 10. A distribution of multivariate normal random numbers was then generated for each patient by means of the MATLAB function *mvnrnd*, given the mean values of native frequency and bandwidth, and the covariance matrix as inputs. Finally, a normalized multivariate normal probability density function was generated in MATLAB by means of the *mvnpdf* function, given the previously computed distribution of multivariate normal random numbers, the mean values of native frequency and bandwidth, and the covariance matrix as inputs.

To evaluate the performance of classifiers based on the three features introduced in this article, each patient was characterized with the mean values of native frequency, bandwidth, and total intensity of its B-lines (the average values of the B-lines observed in the patient). We referred to these parameters as "mean native frequency," "mean bandwidth," and "mean total intensity."

To evaluate the statistical significance of each feature, an analysis of variance (ANOVA) test was performed between the fibrotic and nonfibrotic groups. In particular, the mean parameters were investigated.

The ANOVA tests were performed by means of the MATLAB function *anova1*.

### D. Classifiers

To objectively evaluate the potentiality of the mean native frequency, mean bandwidth, and mean total intensity for discriminating fibrotic patients, we trained and tested two different well-known classifiers, i.e., support vector machines (SVMs) with Gaussian kernels [31] and decision trees [32]. More specifically, both the SVMs and decision trees classifiers were implemented in MATLAB by means of the *fitcsvm* and *fitctree* functions, respectively. Each classifier was trained and tested by using $k$-fold cross validation, with $k$ ranging from 2 to 26, where 26 is the number of samples (patients) in the data set. Since $k$-fold cross validation strictly depends on the randomly chosen groups, we performed a repeated $k$-fold cross validation by repeating 20 times the cross validation process for each value of $k$. Then, the performance results (accuracy, and specificity and sensitivity with respect to the fibrotic group) were averaged to obtain more objective measures of performance. To evaluate the classifiers' performance by testing all the possible combinations of the aforementioned features, the process was repeated seven times, i.e., by testing each feature separately, each couple of features, and the three features together. Finally, an empirical evaluation with respect to the classifiers' parameters was performed, and the SVM (*BoxConstraint* and *KernelScale*, set to 10 and 1, respectively) and the decision tree (*MinParentSize* set to 10) having the best accuracy were chosen. Moreover, an empirically defined binary classifier was introduced to show the best performance achievable with this data set. This classifier was defined by visually observing the samples' distribution in a bidimensional plot with the mean native frequency and bandwidth as coordinates and setting two bounds (lower and upper) for each of these two features. Successively, to achieve the best specificity, an additional empirical upper bound was defined for the mean total intensity. Since the empirically binary classifier perfectly overfit the data set, it obviously outperforms the SVM and the decision tree. The scope of this classifier is in fact to show

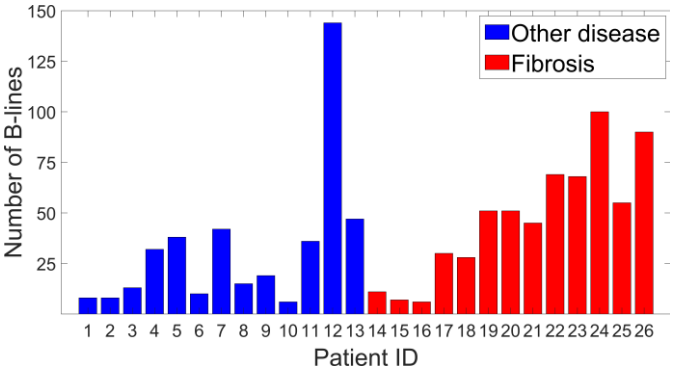


Fig. 2. Number of B-lines for each patient. The patients with ID from 1 to 13 (blue bars) are diagnosed as nonfibrotic, whereas the patients with ID from 14 to 26 (red bars) are diagnosed as fibrotic.

what the best achievable performance for this data set is and not to define a reproducible classification criterion.

## III. Results

### A. B-Lines' Initial Evaluation

Fig. 2 shows how many B-lines were detected for each patient, highlighting the difference between the patients suffering from PF (611 B-lines) and the others (418 B-lines). Indeed, even though the number of B-lines is generally greater in patients suffering from PF, some of these patients (ID 14, 15, and 16) present a low number of artifacts. Fig. 3 (top and center) shows how the distributions representing the fibrotic patients are located within a specific range of native frequency and bandwidth, whereas the group of patients affected by other diseases is more heterogeneous and covers a larger range. To evaluate the possibility to discriminate the fibrotic patients from the others, each patient was represented as a point in a 2-D plane with the mean native frequency and mean bandwidth as coordinates (see Fig. 3 at the bottom). Then, a binary classifier was empirically defined so that the patients with the mean native frequency between 3.95 and 5.00 MHz and the mean bandwidth between 2.3 and 3.5 MHz are classified as fibrotic. Despite the simplicity of this classifier, a sensitivity approximately equal to 92% and a specificity about 77% were achieved. To further improve the classification performance, the mean total intensity was evaluated. Indeed, the literature suggests that B-lines probably originate from acoustic traps, whose characteristics depend on the pathologies affecting the lung parenchyma [28]. In particular, in PF, these traps are composed of fibrotic content, whose attenuation is significantly higher than fluids, such as water and blood. Hence, it is expected that B-lines would generally show a lower intensity in fibrotic patients [28], as observable in Fig. 4. This concept is further confirmed by the histograms of the total intensity depicted in Fig. 5 (top). The mean of the histogram representing the nonfibrotic patients is indeed significantly higher (−0.64 dB) than fibrotic patients (−4.76 dB). As a consequence, to exclude patients with more intense B-lines, a threshold empirically fixed at 1.6 dB was applied to the mean total intensity. The introduction of this new discrimination criterion allowed the correct classification of six nonfibrotic patients, two of whom were previously misclassified. Therefore, as observable in Fig. 5 (bottom), thanks to the mean total

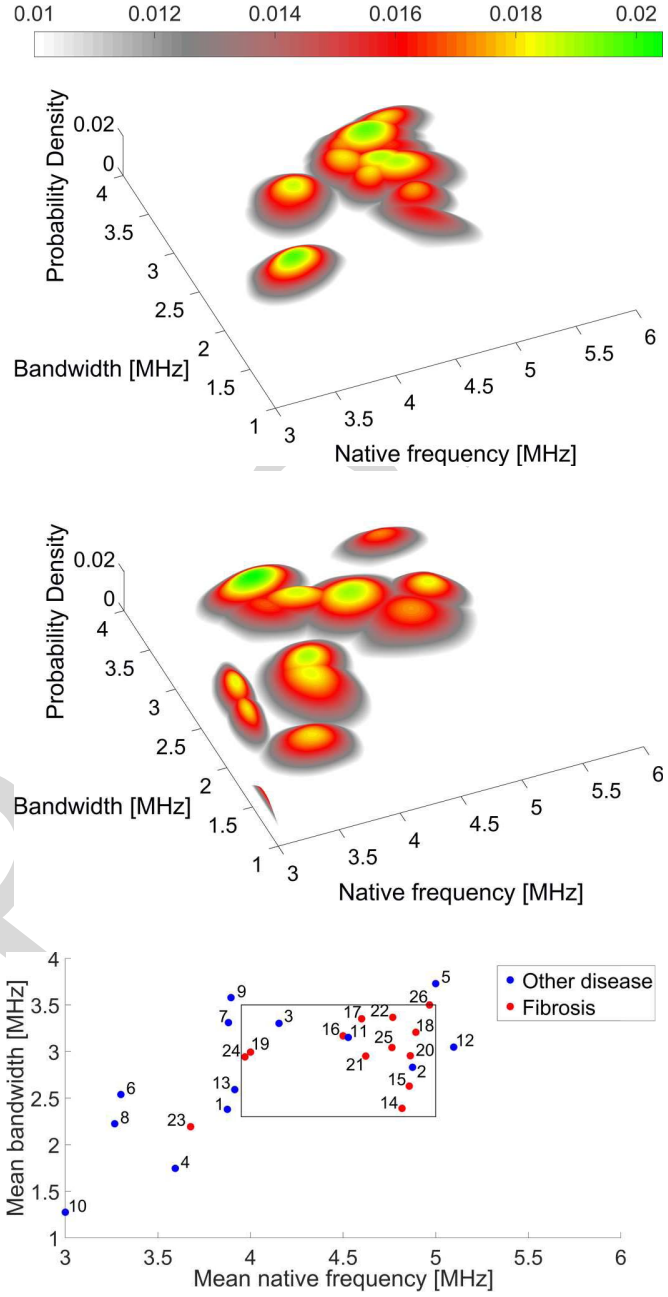


Fig. 3. Gaussian distributions representing the 13 fibrotic patients (top) and the 13 nonfibrotic patients (center). The Gaussian distributions were generated by considering the mean native frequency, the mean bandwidth, and the covariance matrix of native frequency and bandwidth of B-line artifacts. The covariance matrix was divided by a factor of 10 to improve the visualization. The 26 patients are jointly depicted in the 2-D plot (bottom), where the *x*-axis and the *y*-axis represent the mean native frequency and the mean bandwidth of the B-lines observed in each patient, respectively. The patient IDs are written near the corresponding points. The patients within the black box are classified as fibrotic by the empirically defined binary classifier.

intensity evaluation, the specificity increased from about 77% to approximately 92%.

### B. Classifiers' Performance

Fig. 6 shows the performance of the selected classifiers (SVM and decision tree) in discriminating fibrotic patients

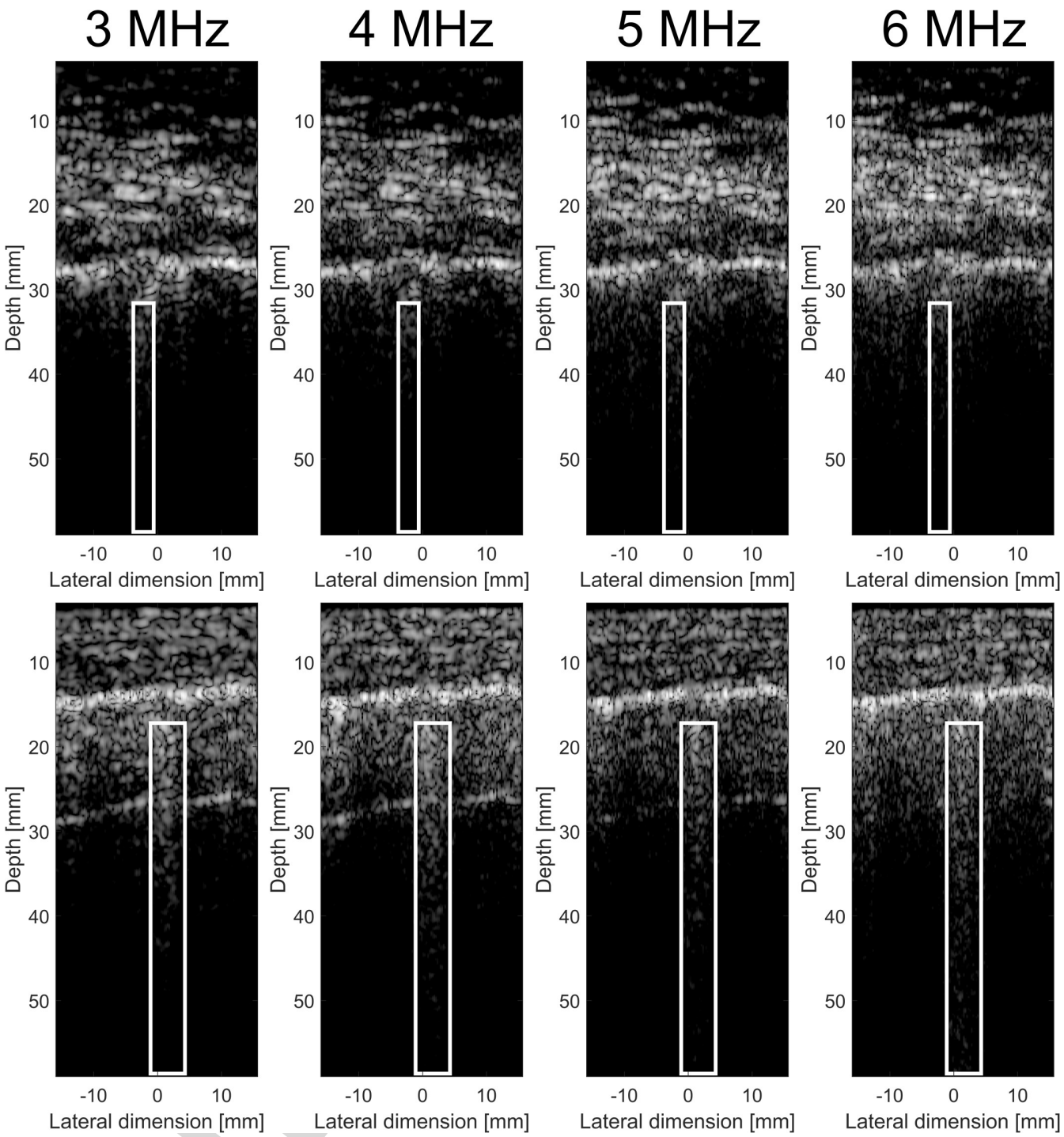


Fig. 4. Multifrequency images of the fibrotic patient labeled with ID 16 (top) and the nonfibrotic patient labeled with ID 7 (bottom). The regions of interest ($ROI_B$) that were used to compute the total intensity are represented as white boxes. The images are shown with a 35-dB dynamic range.

from the other group. The best accuracy was obtained when the decision tree was used. In particular, the maximum accuracy (76.9%) was achieved by exploiting the mean native frequency (singular feature) or the mean native frequency together with the bandwidth (multiple features) as parameters. The SVM's accuracy trend is similar, even though the achieved accuracy (maximum value equal to 74% when only the mean native frequency was used as feature) is lower than for the decision tree. The performance of both the decision tree and the SVM decreases when all the features were exploited (maximum accuracy about 72.5% and 68.3%, respectively). This accuracy decrement is likely due to the higher complexity of the model, whose discrimination power hardly increases with such a low number of samples. The decision tree's sensitivity is generally higher than the SVM (maximum sensitivity is, respectively, about 75.8% with the mean native frequency and mean total intensity as features and 71.5% with only the mean native frequency as feature), whereas its maximum specificity is

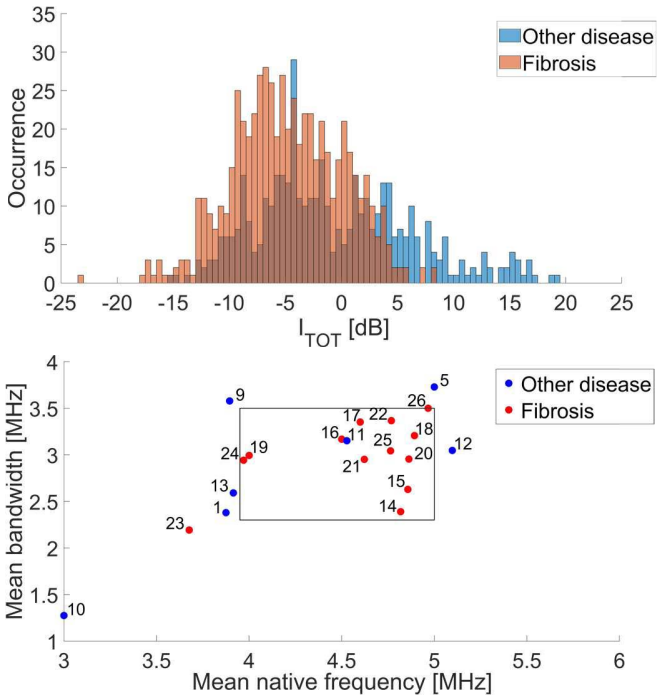


Fig. 5. Histograms of the total intensity for fibrotic (red bars) and nonfibrotic (blue bars) patients are depicted on the top. The occurrence represents the number of B-lines as a function of the total intensity (*x*-axis). The 2-D plot (bottom) represents the patients as a function of the mean native frequency and mean bandwidth of the B-lines observed in each patient after the application of a 1.6-dB threshold to the mean total intensity. The nonfibrotic patients are reduced to 7, with a consequent increase of specificity to 92%. The patient IDs are written near the corresponding points. The patients within the black box are classified as fibrotic by the empirically defined binary classifier.

lower than the SVM (respectively, about 86.64% and 92.24% with the mean total intensity as feature).

### C. Features' Statistical Analysis

The *p*-values obtained by performing the ANOVA test to compare the overall difference between the fibrotic and nonfibrotic groups are 0.0236, 0.3190, and 0.0056 for the mean native frequency, mean bandwidth, and mean total intensity, respectively.

## IV. Conclusion and Discussion

Due to its portability, cost-effectiveness, and safety, lung ultrasonography represents nowadays a key instrument to provide clinicians with important information on the state of the lung surface. The aforementioned characteristics make LUS extremely useful especially in emergency and critical care settings [6], such as in the monitoring of COVID-19 pneumonia [23], [24]. The potentials of LUS in supporting clinicians during the diagnostic process have been studied since the 1990s, when, for the first time, the vertical artifacts known as B-lines were observed in patients with alveolar interstitial syndrome [7].

B-lines appear generally different in the presence of different pathological conditions of the lung [6]. For example, the possibility to qualitatively differentiate cardiogenic from

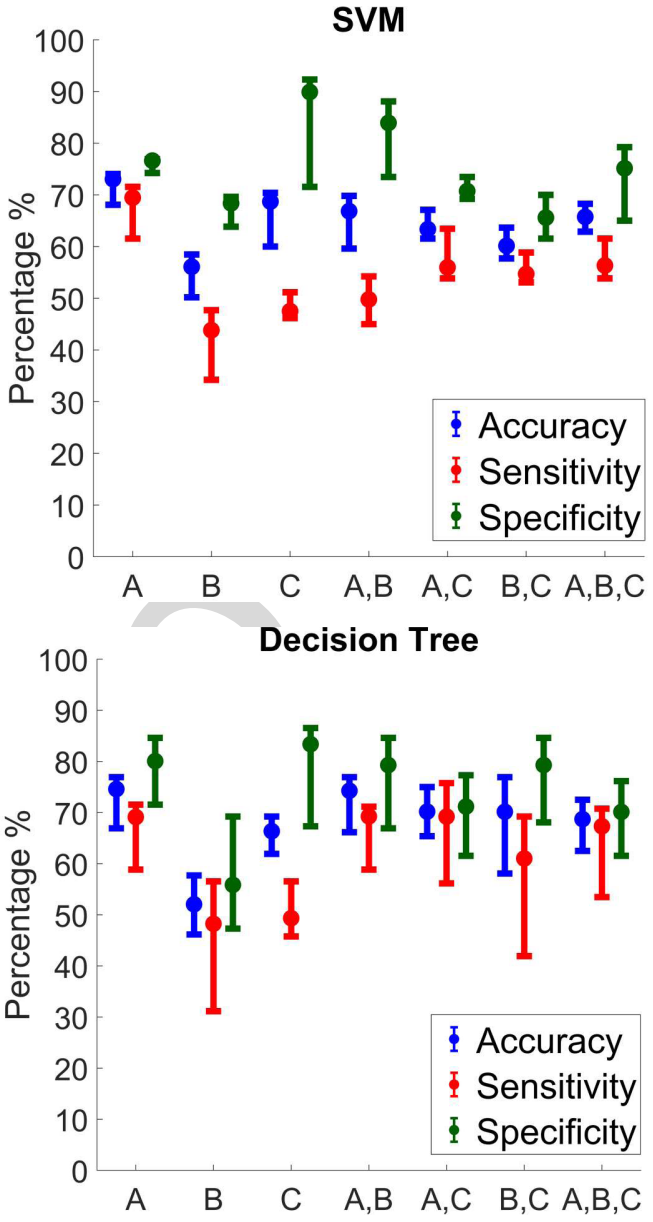


Fig. 6. Performance of the selected SVM and decision tree is shown. The accuracy, sensitivity with respect to the fibrotic group, and specificity with respect to the fibrotic group are represented as error bars in blue, red, and green, respectively. The upper and lower values of each error bar represent the maximum and minimum values of accuracy, sensitivity, and specificity obtained by varying *k* parameter of *k*-fold cross validation. The points of the error bars represent the average value of the performance obtained by averaging the performance values obtained with *k*-fold cross validation, with *k* ranging from 2 to 26. The *x*-axis represents the features exploited in the selected model, where *A* is the mean native frequency, *B* is the mean bandwidth, and *C* is the mean total intensity. When multiple features were exploited, a comma is used in the *x*-axis to separate them (e.g., *A*, *B*).

pneumogenic interstitial syndrome is well recognized in the literature [6]. The appearance of B-lines is indeed different in these two groups of pathologies, likely due to different shape and size of the acoustic traps that form on the diseased lung surface [28].

The characteristics of acoustic traps could be detected by analyzing the frequency spectrum of B-lines [16], which were

already proved to be frequency dependent [18]. Of particular interest is the discrimination of patients affected by PF, which is characterized by more attenuated and diffused B-lines, probably due to the heterogeneity and composition of acoustic traps [28].

In this article, we have presented a study investigating the potentials of a B-line frequency characterization method with respect to the differentiation of patients affected by PF. We exploited the multifrequency approach introduced in [18], which provided images of the same region acquired with four different center frequencies. The raw RF data acquired from 26 patients, half of whom affected by PF, were then processed and the total intensity parameter was extracted to quantitatively evaluate the B-line intensity. To characterize all the 1029 B-lines, the total intensity was evaluated as a function of frequency, hence determining the native frequency and the bandwidth of each B-line.

The results show differences between the vertical artifacts observed in fibrotic patients with respect to patients affected by other diseases (Figs. 3 and 4). Indeed, while fibrotic patients are more homogeneously distributed within a specific range of native frequencies and bandwidths (native frequency near the average of the investigated frequency range, i.e., 4.5 MHz, and bandwidth within 2.3 and 3.5 MHz), the other group is characterized by a more heterogeneous distribution covering a wider range (Fig. 3). This is consistent with the pathological conditions affecting the two groups of patients. The nonfibrotic patients are in fact affected by different diseases (e.g., pneumonia, COPD, and pulmonary hypertension), whereas the fibrotic patients are specifically characterized by their histopathological pattern, which is almost unique. The heterogeneity of the nonfibrotic group is further confirmed by the total intensity histogram (Fig. 5 at the top), whose standard deviation is relatively higher (6.9 dB) compared to the other group (4.9 dB). Moreover, the mean total intensity of all the B-lines representing fibrotic patients is significantly lower (−4.76 dB) than the mean value of the nonfibrotic group (−0.64 dB). This difference is likely associated with the physical composition of acoustic traps, which, in several diseases different from PF, are generally consisted of less attenuating media (e.g., water and blood) than fibrotic tissue [8], [9]. As further confirmation, the introduction of a threshold to the mean total intensity allowed the specificity of the empirically defined binary classifier to be improved up to 92% (+15% compared to the binary classification that consider as discriminating parameters only the mean native frequency and bandwidth).

The discrimination power of the three features (native frequency, bandwidth, and total intensity) is reported by the statistical analysis. When investigating the overall differences between the PF and non-PF populations, a $p$-value equal to 0.0236, 0.3190, and 0.0056 for the mean native frequency, mean bandwidth, and mean total intensity was obtained, respectively. Considering a threshold to $p$-values at 0.05, both the native frequency and total intensity are significant for discriminating the two groups. Differently, the bandwidth is not. Furthermore, the statistical analysis' results seem to be consistent with the performance achieved by the SVM and decision tree (Fig. 6), where the native frequency has the strongest discrimination power, followed by the total intensity and finally the bandwidth.

In conclusion, the quantitative evaluation of B-lines by means of both the multifrequency analysis and the total intensity is potentially able to discriminate fibrotic patients. These promising results could open to the definition of an ultrasound imaging technique specifically designed for the lungs. However, there exist cases where the artifactual pattern is similar to fibrotic patients and, hence, the analyzed discrimination parameters (total intensity, native frequency, and bandwidth) are not sufficient. As a consequence, further investigation is necessary. Of particular interest could be the analysis of patients with specific diseases, such as cardiogenic pulmonary edema (CPE), that show artifactual and histopathological patterns extremely different from fibrotic patients. Through the evaluation of a larger group of patients affected by PF and another group of patients affected by CPE, the potentiality of the method described in this article could be further explored.

## References


[1] *The Global Impact of Respiratory Disease*, 2nd ed, Forum of International Respiratory Societies, European Respiratory Society, Sheffield, U.K., 2017.

[2] *Coronavirus Disease 2019 Situation Report—128*, World Health Organization, Geneva, Switzerland, 2020.

[3] J. H. Ryu *et al.*, "Idiopathic pulmonary fibrosis: Evolving concepts," *Mayo Clinic Proc.*, vol. 89, no. 8, pp. 1130–1142, Aug. 2014.

[4] F. J. Martinez *et al.*, "Idiopathic pulmonary fibrosis," *Nature Rev. Disease Primers*, vol. 3, no. 1, 2017, Art. no. 17074.

[5] J. M. Oldham and I. Noth, "Idiopathic pulmonary fibrosis: Early detection and referral," *Respiratory Med.*, vol. 108, no. 6, pp. 819–829, Jun. 2014.

[6] G. Soldati, M. Demi, A. Smargiassi, R. Inchingolo, and L. Demi, "The role of ultrasound lung artifacts in the diagnosis of respiratory diseases," *Expert Rev. Respiratory Med.*, vol. 13, no. 2, pp. 163–172, Feb. 2019.

[7] D. Lichtenstein, G. Mézière, P. Biderman, A. Gepner, and O. Barré, "The comet-tail artifact: An ultrasound sign of alveolar-interstitial syndrome," *Amer. J. Respiratory Crit. Care Med.*, vol. 156, no. 5, pp. 1640–1646, Nov. 1997.

[8] G. Soldati, *2.17—Biomedical Applications of Ultrasound*, A. B. T.-C. B. P. Brahme, Ed. Oxford, U.K.: Elsevier, 2014, pp. 401–436.

[9] G. Soldati, M. Demi, R. Inchingolo, A. Smargiassi, and L. Demi, "On the physical basis of pulmonary sonographic interstitial syndrome," *J. Ultrasound Med.*, vol. 35, no. 10, pp. 2075–2086, Oct. 2016.

[10] D. A. Lichtenstein and G. A. Mezière, "Relevance of lung ultrasound in the diagnosis of acute respiratory Failure*: The BLUE protocol," *Chest*, vol. 134, no. 1, pp. 117–125, Jul. 2008.

[11] R. Copetti, G. Soldati, and P. Copetti, "Chest sonography: A useful tool to differentiate acute cardiogenic pulmonary edema from acute respiratory distress syndrome," *Cardiovascular Ultrasound*, vol. 6, no. 1, p. 16, Apr. 2008.

[12] E. Picano and P. A. Pellikka, "Ultrasound of extravascular lung water: A new standard for pulmonary congestion," *Eur. Heart J.*, vol. 37, no. 27, pp. 2097–2104, May 2016.

[13] L. Gargani *et al.*, "Ultrasound lung comets in systemic sclerosis: A chest sonography hallmark of pulmonary interstitial fibrosis," *Rheumatology*, vol. 48, no. 11, pp. 1382–1387, Aug. 2009.

[14] G. Soldati *et al.*, "Lung ultrasonography may provide an indirect estimation of lung porosity and airspace geometry," *Respiration*, vol. 88, no. 6, pp. 458–468, 2014.

[15] L. Avruch and P. L. Cooperberg, "The ring-down artifact.," *J. Ultrasound Med.*, vol. 4, no. 1, pp. 21–28, Jan. 1985.

[16] M. Demi, R. Prediletto, G. Soldati, and L. Demi, "Physical mechanisms providing clinical information from ultrasound lung images: Hypotheses and early confirmations," *IEEE Trans. Ultrason., Ferroelectr., Freq. Control*, vol. 67, no. 3, pp. 612–623, Mar. 2020.

[17] G. Soldati, V. Giunta, S. Sher, F. Melosi, and C. Dini, "'Synthetic' comets: A new look at lung sonography," *Ultrasound Med. Biol.*, vol. 37, no. 11, pp. 1762–1770, Nov. 2011.

[18] L. Demi, W. van Hoeve, R. J. G. van Sloun, G. Soldati, and M. Demi, "Determination of a potential quantitative measure of the state of the lung using lung ultrasound spectroscopy," *Sci. Rep.*, vol. 7, no. 1, p. 12746, Dec. 2017.

[19] G. Volpicelli *et al.*, "International liaison committee on lung ultrasound (ILC-LUS) for international consensus conference on lung ultrasound (ICC-LUS). International evidence based recommendations for point-of-care lung ultrasound," *Intensive Care Med*, vol. 38, pp. 557–591, Jan. 2012.

[20] L. Gargani, "Lung ultrasound: A new tool for the cardiologist," *Cardiovascular Ultrasound*, vol. 9, no. 1, p. 6, Feb. 2011.

[21] L. Gargani, "Ultrasound of the lungs: More than a room with a view," *Heart Fail. Clin.*, vol. 15, no. 2, pp. 297–303, 2019.

[22] F. Corradi *et al.*, "Computer-aided quantitative ultrasonography for detection of pulmonary edema in mechanically ventilated cardiac surgery patients," *Chest*, vol. 150, no. 3, pp. 640–651, Sep. 2016.

[23] G. Soldati *et al.*, "Is there a role for lung ultrasound during the COVID-19 pandemic," *J. Ultrasound Med.*, to be published.

[24] G. Soldati *et al.*, "Proposal for international standardization of the use of lung ultrasound for COVID-19 patients; A simple, quantitative, reproducible method," *J. Ultrasound Med.*, to be published.

[25] K. Mohanty, J. Blackwell, T. Egan, and M. Müller, "Characterization of the lung parenchyma using ultrasound multiple scattering," *Ultrasound Med. Biol.*, vol. 43, no. 5, pp. 993–1003, May 2017.

[26] X. Zhang *et al.*, "Lung ultrasound surface wave elastography: A pilot clinical study," *IEEE Trans. Ultrason., Ferroelectr., Freq. Control*, vol. 64, no. 9, pp. 1298–1304, Sep. 2017.

[27] L. Demi, T. Egan, and M. Müller, "Lung ultrasound imaging, a technical review," *Appl. Sci.*, vol. 10, no. 2, p. 462, Jan. 2020.

[28] G. Soldati, A. Smargiassi, L. Demi, and R. Inchingolo, "Artifactual lung ultrasonography: It is a matter of traps, order, and disorder," *Appl. Sci.*, vol. 10, no. 5, p. 1570, Feb. 2020.

[29] P. Tortoli, L. Bassi, E. Boni, A. Dallai, F. Guidi, and S. Ricci, "ULA-OP: An Advanced Open Platform for Ultrasound Research," *IEEE Trans. Ultrason., Ferroelectr., Freq. Control*, vol. 56, pp. 2207–2216, Oct. 2009.

[30] T. L. Szabo, *Attenuation*, E. Szabo, Ed. Boston, MA, USA: Academic, 2014, pp. 81–119.

[31] N. Cristianini and J. Shawe-Taylor, *An Introduction to Support Vector Machines and Other Kernel-based Learning Methods*. Cambridge, U.K.: Cambridge Univ. Press, 2000.

[32] L. Breiman, J. H. Friedman, R. A. Olshen, and C. J. Stone, *Classification and Regression Trees*. Boca Raton, FL, USA: CRC Press, 1984.